

# Chemical Science

Accepted Manuscript



This article can be cited before page numbers have been issued, to do this please use: J. Gong, K. Ma, Y. Tian, Z. Zhao, Q. Cheng, T. Ding, J. Zhang, L. Zheng, Z. Jiang, T. Abe, N. Tsubaki and X. Li, *Chem. Sci.*, 2019, DOI: 10.1039/C9SC00015A.



This is an Accepted Manuscript, which has been through the Royal Society of Chemistry peer review process and has been accepted for publication.

Accepted Manuscripts are published online shortly after acceptance, before technical editing, formatting and proof reading. Using this free service, authors can make their results available to the community, in citable form, before we publish the edited article. We will replace this Accepted Manuscript with the edited and formatted Advance Article as soon as it is available.

You can find more information about Accepted Manuscripts in the [author guidelines](#).

Please note that technical editing may introduce minor changes to the text and/or graphics, which may alter content. The journal's standard [Terms & Conditions](#) and the ethical guidelines, outlined in our [author and reviewer resource centre](#), still apply. In no event shall the Royal Society of Chemistry be held responsible for any errors or omissions in this Accepted Manuscript or any consequences arising from the use of any information it contains.

## Journal Name

## ARTICLE

# Achieving efficient and robust catalytic reforming on dual-sites of Cu species†

Kui Ma,<sup>a,b</sup> Ye Tian,<sup>a,b</sup> Zhi-Jian Zhao,<sup>a,c</sup> Qingpeng Cheng,<sup>a,b</sup> Tong Ding,<sup>a,b</sup> Jing Zhang,<sup>d</sup> Lirong Zheng,<sup>d</sup> Zheng Jiang,<sup>e</sup> Takayuki Abe,<sup>f</sup> Noritatsu Tsubaki,<sup>g</sup> Jinlong Gong<sup>\*a,c</sup> and Xingang Li<sup>\*a,b</sup>

Received 00th January 20xx,  
Accepted 00th January 20xx

DOI: 10.1039/x0xx00000x

www.rsc.org/

Catalytic reforming provides practical technique for on-board hydrogen production in fuel cells applications. The high energy density, easy transportation and non-toxicity of biomass-derived dimethyl ether (bio-DME) offer potential to replace methanol for on-board steam reforming (SR). Presently, the reaction mechanism over conventional Cu-based SR catalysts remains elusive, limiting the rational design of highly efficient reforming systems. Herein, we build a catalytic system for bio-DME SR with dual-sites of Cu species, i.e., Cu<sup>+</sup> and Cu<sup>0</sup> sites, and achieve a record-high H<sub>2</sub> production rate of 1145 mol kg<sup>-1</sup> cat h<sup>-1</sup>. Via regulating the ratios of the dual-sites of Cu, we clearly describe cut molecular understandings on SR. And we discover that the substantially boosted activity is induced by a new Cu<sup>+</sup>-determined reaction path substituting of the conventional Cu<sup>0</sup>-determined path. Intrinsically, Cu<sub>2</sub>O can act as physical spacer and hydroxyl consumer to suppress the aggregation of metallic Cu species in SR. Due to the unique structure of metallic Cu surrounded by Cu<sub>2</sub>O, the catalyst exhibits robust catalytic performance even after severe thermal treatment. These findings open a new avenue for designing efficient catalytic reforming systems with commercially potential.

## Introduction

Hydrogen, a renewable resource with a high energy density (142 MJ kg<sup>-1</sup>), is consumed today as a chemical raw material (about 5×10<sup>10</sup> kg per year worldwide).<sup>1</sup> As the core of the hydrogen economy, fuel cells running on hydrogen are attractive power supplies for versatile applications.<sup>2, 3</sup> The required hydrogen comes from a stable on-board production system, ensuring its safe storage and transportation.<sup>4, 5</sup> Recently, the development of technologies for converting biomass has resuscitated the surge of reforming renewable oxygenated hydrocarbons, e.g., methanol, ethanol, dimethyl ether (DME), and glycerol, with H<sub>2</sub>O for on-board hydrogen production.<sup>6–8</sup> In view of the mild SR conditions, methanol and DME that without C–C bonds are the primary choices.<sup>9</sup> The usage of DME can release hydrogen with a higher gravimetric

density of 26.1 wt.% than methanol (18.8 wt.%). As the European project BioDME has been industrially built and operated in Sweden, bio-DME is becoming a potential reforming feed to replace the traditional methanol.<sup>10, 11</sup> The non-toxicity of DME offers another important advantage. DME SR is an integrated technology consisting of hydrolysis of DME to methanol over solid acid catalysts, and subsequently methanol SR over metal catalysts. Currently, γ-Al<sub>2</sub>O<sub>3</sub> is the commonly used acid catalyst for DME hydrolysis operated above 300 °C,<sup>12</sup> requiring higher operating temperatures for the followed SR. And copper-based catalysts have been intensively explored in reforming reactions with inherent drawback of thermal deactivation by metal-particle growth.<sup>13</sup>

It is commonly perceived that Cu<sup>0</sup> is primary and indispensable for SR,<sup>14, 15</sup> bringing debate about the role of Cu<sup>+</sup>. Some researchers have proposed that Cu<sup>+</sup> is active in suppressing by-product of carbon monoxide (CO) from reverse water-gas shift, the main side reaction in SR.<sup>16–18</sup> However, the others still suggest that Cu<sup>+</sup> could directly catalyze the steam reforming, and speculate that there may exist an optimum cooperation between Cu<sup>0</sup> and Cu<sup>+</sup> to boost activities,<sup>19–21</sup> but lacking effective evidences. Currently, Cu<sup>+</sup> species are usually introduced through additive of metal oxides in Cu-based catalysts, and self-redox of copper species under feed and reaction conditions.<sup>22–25</sup> The complexity of these systems impairs efforts to identify the exact role of copper. In this regard, the copper phyllosilicates [Cu<sub>2</sub>Si<sub>2</sub>O<sub>5</sub>(OH)<sub>2</sub>], providing stable Cu<sup>+</sup> species under hydrogen-rich conditions in catalytic hydrogenation,<sup>26–28</sup> may be adopted as a controllable Cu<sup>+</sup>-supplier to investigate SR mechanisms. However, the tendency of Cu nanoparticles (NPs) to grow into larger crystallites is an impediment for the stable performance of Cu-based catalysts, especially for that without

<sup>a</sup> School of Chemical Engineering & Technology, Tianjin University; Collaborative Innovation Center of Chemical Science and Engineering (Tianjin), Tianjin 300072, China.

<sup>b</sup> Tianjin Key Laboratory of Applied Catalysis Science & Engineering, Tianjin 300072, China.

<sup>c</sup> Key Laboratory for Green Chemical Technology of Ministry of Education, Tianjin 300072, China.

<sup>d</sup> Beijing Synchrotron Radiation Facility, Institute of High Energy Physics, Chinese Academy of Sciences, Beijing 100049, China.

<sup>e</sup> Shanghai Synchrotron Radiation Facility, Shanghai Institute of Applied Physics, Chinese Academy of Sciences, Shanghai 201800, China.

<sup>f</sup> Hydrogen Isotope Research Center, University of Toyama, Gofuku 3190, Toyama 930-8555, Japan.

<sup>g</sup> Department of Applied Chemistry, School of Engineering, University of Toyama, Gofuku 3190, Toyama 930-8555, Japan.

† Electronic Supplementary Information (ESI) available. See DOI: 10.1039/x0xx00000x



promoters. Intrinsically below the Tammann temperature of copper (407 °C), the aggregation of Cu NPs is mainly induced by Ostwald ripening occurring across the support surface through the functional groups (e.g. hydroxyl).<sup>29</sup> It is another stumbling block in further Cu-based catalysts design.

This paper describes the design and fabrication of a hierarchical Cu-Si system with dual-sites of Cu species (denoted as Cu-AE) via vacuum-rotary ammonia evaporation method by employing SBA-15 as the silicon source. The ordered three-dimensional (3D) mesoporous channels of SBA-15 can improve molecular diffusion, and restrict the growth of copper NPs. As described in Fig. 1A, the well-ordered  $\equiv\text{Si-OH}$  sites on SBA-15 and vacuum condition facilitate the dispersion and uniform arrangement of the Cu species.<sup>30</sup> Consequently, CuO nanoparticles (NPs) dispersing into  $\text{Cu}_2\text{Si}_2\text{O}_5(\text{OH})_2$  nanotubes (NTs) are successfully developed on SBA-15. After reduction, the metallic Cu NPs are generated from the CuO NPs, while the  $\text{Cu}_2\text{O}$  NPs are from the surrounding  $\text{Cu}_2\text{Si}_2\text{O}_5(\text{OH})_2$  NTs. Basing on this synthesis mechanism, we tune the dual-sites of copper to quantify their contributions on SR, and achieve a record-high  $\text{H}_2$  production rate of  $1145 \text{ mol kg}^{-1}_{\text{cat}} \text{ h}^{-1}$  with the structure of metallic Cu surrounded by  $\text{Cu}_2\text{O}$ . We also discover that the formation of  $\text{Cu}_2\text{O}$  consumes the hydroxyl groups on the support, which retards the Ostwald ripening of metallic Cu, thereby leading to a robust SR performance.

## Results and discussion

The TEM images of 25Cu-AE in Fig. 1B-D are obtained to illustrate the synthetic procedure. As indicated by the FTIR and UV-Raman results (Fig. S1), abundant  $\equiv\text{Si-OH}$  groups (the  $\nu_{\text{Si-OH}}$  vibration at  $958 \text{ cm}^{-1}$ )<sup>31</sup> exist on the  $\text{SiO}_4$  tetrahedron-shaped matrix of the mesoporous SBA-15 (Fig. 1B). After ammonia evaporation, the disappearance of the  $\nu_{\text{Si-OH}}$  vibration band in 25Cu-AE implies that the  $\equiv\text{Si-OH}$  groups are consumed during the  $\text{Cu}_2\text{Si}_2\text{O}_5(\text{OH})_2$  formation. On 25Cu-AE, the NPs are CuO, while the NTs lacking of lattice fringe are  $\text{Cu}_2\text{Si}_2\text{O}_5(\text{OH})_2$  (Fig. 1C).<sup>32</sup> This formation mechanism is also adapted to the other Cu-AE catalysts with different Cu loadings. The XRD and X-ray absorption near-edge

structure (XANES) results also verify the coexistence of  $\text{Cu}_2\text{Si}_2\text{O}_5(\text{OH})_2$  and CuO in Cu-AE catalysts (Fig. S2).

Semi-quantitatively, we adopted linear combination fitting (LCF) of the XANES spectra (Fig. S3) to estimate the contents of  $\text{Cu}_2\text{Si}_2\text{O}_5(\text{OH})_2$  in the catalysts. It shows a volcano-type following the increase of the Cu content and maximizes at 25Cu-AE (Table S1). Intuitively, in Fig. S4A, CuO NPs continuously enrich with the increase of the copper content in the catalysts, and eventually cap the  $\text{Cu}_2\text{Si}_2\text{O}_5(\text{OH})_2$  NTs. From the low-angle XRD patterns in Fig. S5, all the samples present three well-resolved diffractions at  $2\theta$  of 0.5–3.0, which can be indexed to the ordered hexagonal lattice (p6mm) of SBA-15.<sup>30</sup> Noticeably, the diffraction peaks of the Cu-AE catalysts shift to higher angles compared with the pristine SBA-15, reflecting a slight contraction of the unit cell. This phenomenon is contributed by the partial destruction of the ordered pore structure of SBA-15 due to the dissolution of silica during the preparation process, as can be directly observed by TEM shown above. Here, the existence of these characteristic low-angle diffraction peaks of Cu-AE suggests that most of the channels of SBA-15 are still preserved. Furthermore, the Cu-AE catalysts show the weaker  $d_{100}$  intensity, indicating the copper loading in the mesopore channels reduces X-ray diffraction.<sup>33, 34</sup> Based on the above results, the schematic illustrations of the Cu species distribution with the increased Cu loading are proposed in Fig. S4C. Summarily, the 25Cu-AE possesses

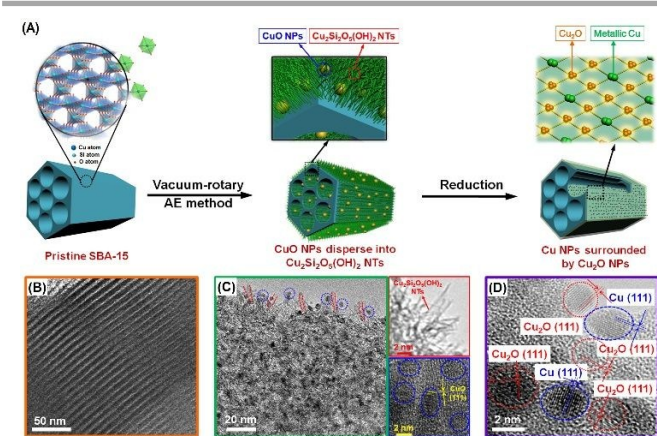


**Fig. 1** (A) Schematic procedure for the synthesis of the Cu-AE catalysts; TEM images of (B) the pristine SBA-15, (C) calcined and (D) reduced 25Cu-AE catalyst.

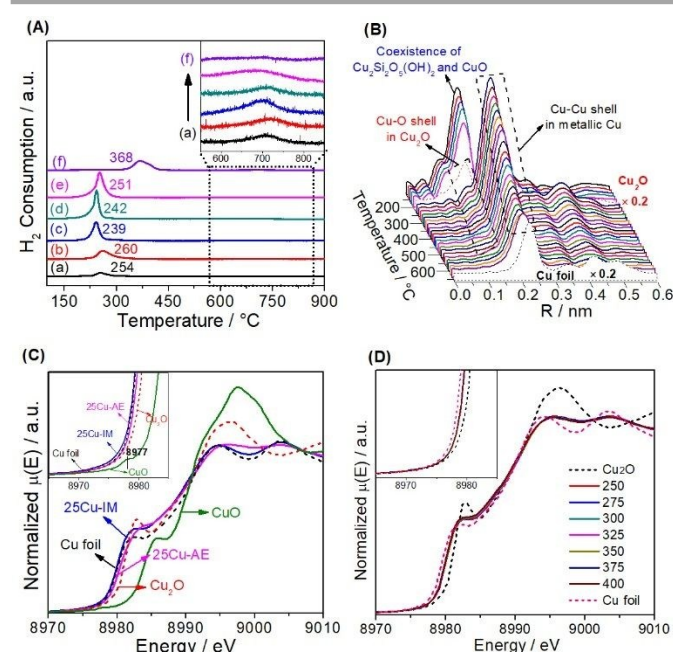


**Fig. 2** (A)  $\text{H}_2$ -TPR profiles of (a) 10Cu-AE, (b) 20Cu-AE, (c) 25Cu-AE, (d) 30Cu-AE, (e) 40Cu-AE, and (f) 25Cu-IM, the inset shows the reduction of  $\text{Cu}^+$  in copper phyllosilicates; (B) Temperature-resolved *in-situ* RSFs of Cu K-edge for 25Cu-AE in 5%  $\text{H}_2/\text{N}_2$  from RT to 650 °C; (C) *In-situ* steady-state XANES spectra of Cu K-edge for the reduced 25Cu-AE and 25Cu-IM catalysts in 5% reactants ( $n(\text{CH}_3\text{OH})/n(\text{H}_2\text{O}) = 1/2$ ) in  $\text{N}_2$  at 400 °C, the inset shows the amplified curves; (D) *In-situ* temperature-resolved XANES spectra of Cu K-edge for the reduced 25Cu-AE catalyst under reaction conditions: 5% reactants ( $n(\text{CH}_3\text{OH})/n(\text{H}_2\text{O}) = 1/2$ ) in  $\text{N}_2$ , from 250 to 400 °C at interval of 25 °C; the inset shows the amplified curves.



the well-proportioned and uniformly arranged  $\text{Cu}_2\text{Si}_2\text{O}_5(\text{OH})_2$  NTs and CuO NPs.

Upon the reduced Cu-AE catalysts, both the preserved characteristic diffractions of SBA-15 in low-angle XRD patterns (Fig. S6A), and the narrowed size distribution at 4.3 nm (Fig. S7) demonstrate the existence of regular channels. We also observed the  $\text{Cu}_2\text{O}$  (JCPDS No. 05-0667) and metallic Cu (JCPDS No. 04-0836) from wide-angle XRD patterns in Fig. S6B.  $\text{Cu}_2\text{O}$  and metallic Cu originate from the reduction of  $\text{Cu}_2\text{Si}_2\text{O}_5(\text{OH})_2$  and CuO, respectively.<sup>27</sup> Specially, the metallic Cu is surrounded by  $\text{Cu}_2\text{O}$  on 25Cu-AE (Fig. 1D), which is due to the proper proportion of Cu species in the calcined catalysts (Fig. S4). Table S2 gives the physicochemical properties of the catalysts, indicating that we can modulate the physicochemical properties of Cu-AE via tuning the Cu loading. Compared with other catalysts, the Cu-AE catalysts possess the smaller Cu crystal sizes and more accessible surface Cu atoms.

We employed  $\text{H}_2$ -TPR (Fig. 2A) and *in-situ* reduction XAFS (Fig. 2B) to identify the reducibility and copper species of the catalysts. Generally, the reduction of copper phyllosilicates to  $\text{Cu}^+$  and highly dispersed CuO to  $\text{Cu}^0$  occurs at ca. 247–267 °C<sup>28</sup> and 237 °C,<sup>35</sup> respectively. Thus, we attribute the single peak below 300 °C here to the overlap of these two reduction processes. Correspondingly in this range, we observe the co-existence of  $\text{Cu}_2\text{O}$  with the first Cu-O coordination (ca. 0.15 nm) and metallic Cu with the first Cu-Cu coordination (ca. 0.20 nm). The existence of  $\text{Cu}^+$  in the reduced Cu-AE catalysts is also verified by the  $\text{Cu}^+$ -carbonyl band (2122  $\text{cm}^{-1}$ ) observed from the *in-situ* DRIFTS spectrum of CO adsorption (Fig. S8). Notably, the broadening peaks above 600 °C (Inset in Fig. 2A) indicate the further reduction of  $\text{Cu}^+$  to metallic Cu.<sup>35</sup> Simultaneously, the Cu-O coordination peaks decrease, also indicating the gradual reduction of the Cu species to  $\text{Cu}^0$  in Fig. 2B. For 25Cu-IM, the main reduction peak at ca. 368 °C is assigned to the reduction of large CuO particles to metallic Cu.<sup>26</sup>

We also distinguished the superficial copper species of  $\text{Cu}^+$  and  $\text{Cu}^0$  using the Cu LMM Auger kinetic energy peaks<sup>36</sup> at ca. 915.5 and 919.0 eV, respectively, for the reduced catalysts (Fig. S9). The modified Auger parameter (A.P.) values, which represent the summation of the kinetic energy of the Cu LMM Auger electron and the binding energy of the Cu  $2p_{3/2}$  photoelectron, are calculated and summarized in Table S3. The smaller A.P. values of  $\text{Cu}^+$  here (ca.

1848.5 eV) than that of the  $\text{Cu}_2\text{O}$  bulk (ca. 1849.0 eV)<sup>36</sup> are attributed to the electron transfer from  $\text{Cu}^0$  to SBA-15, indicating a strong interaction to keep the  $\text{Cu}^+$  stable. Moreover, the Cu 2p XPS spectra (Fig. S10) before and after single reaction cycle indicates that the change in the chemical environment and content of surface Cu (Table S3) are nearly negligible, also suggesting that the equilibrium between  $\text{Cu}^+$  and  $\text{Cu}^0$  over the reduced Cu-AE catalysts is very stable, and is difficultly broken by the SR reaction. In addition, as summarized in Table S3, the ratio of  $\text{Cu}^+ / (\text{Cu}^0 + \text{Cu}^+)$  decreases with the elevated Cu loading, coinciding with the tendency of calculated surface Cu atoms in Table S2.

Generally, the chemical state of Cu species is sensitive to the environmental atmosphere.<sup>37</sup> We performed *in-situ* steady-state XANES to monitor the chemical state of Cu under reaction conditions. As calibrated by the first derivatives of the K-edge XANES spectra in Fig. S11, the absorption edge at ca. 8980.4 eV of 25Cu-AE in Fig. 2C locates in the middle of Cu foil (8979.4 eV) and  $\text{Cu}_2\text{O}$  (8980.9 eV). Combining with the absence of the pre-edge feature at ca. 8977 eV for  $\text{Cu}^{2+}$  (Inset in Fig. 2C),<sup>38</sup> we conclude that  $\text{Cu}^+$  species indeed exist in 25Cu-AE and maintain stable during the operation. But for 25Cu-IM, its absorption edge location and white line feature are close to Cu foil, indicating the lacking of  $\text{Cu}^+$  in the bulk of 25Cu-IM during the reaction. Fig. 2D shows the *in-situ* temperature-resolved XANES spectra of 25Cu-AE. The curves are quite similar in shape at different reaction temperatures, and their absorption edges locate in the middle of Cu foil and  $\text{Cu}_2\text{O}$ . These results demonstrate that the copper oxidation state has little change in dynamic reactive atmospheres at different reaction temperatures, in accordance with the XPS results from Figs. S9, S10 and Table S3. The above comprehensive characterization results demonstrate a successful synthesis of the catalytic system with tuneable and stable dual-sites of Cu species.

We investigated the catalytic performance and stability of the catalysts after 12-h severe thermal treatment (GHSV = 36,000  $\text{h}^{-1}$ ,  $T = 450$  °C) for DME SR. Table 1 summarizes the performance of the catalysts in a numerical form, and the Table S4 lists the activity of the representative catalysts for DME SR and methanol SR. In Table 1, 25Cu-AE exhibits the higher catalytic activity in comparison with others. It achieves a DME conversion of 100%, CO selectivity of ca.

**Table 1** Catalytic performance for DME SR

Catalysts	Conv. (%)	Y. (%)	Sel. (%)			TOF <sub>H<sub>2</sub></sub> <sup>b</sup> (s <sup>-1</sup> ×10 <sup>-2</sup> )	TOF <sub>DME</sub> <sup>c</sup> (s <sup>-1</sup> ×10 <sup>-3</sup> )
	DME	H <sub>2</sub>	CO	CO <sub>2</sub>	CH <sub>4</sub>	CH <sub>3</sub> OH	
10Cu-AE <sup>a</sup>	58.3±6.8	51.6±9.3	12.5±6.3	85.8±7.9	1.7±0.3	-	7.9±0.4
20Cu-AE <sup>a</sup>	89.0±0.6	80.9±3.3	13.4±3.8	86.3±3.9	0.3±0.1	-	12.1±0.5
25Cu-AE <sup>a</sup>	100.0±0.0	95.0±1.5	10.4±3.0	89.3±2.9	0.3±0.1	-	14.7±0.9
30Cu-AE <sup>a</sup>	96.7±0.7	85.4±2.5	12.4±0.8	87.4±2.0	0.2±0.1	-	11.3±1.0
40Cu-AE <sup>a</sup>	77.5±2.4	69.4±4.0	31.5±7.2	68.0±7.5	0.5±0.2	-	6.1±1.1
25Cu-IM <sup>a</sup>	16.0±0.6	12.5±0.7	41.5±5.9	57.9±6.7	0.6±0.2	5.5×10 <sup>-2</sup>	1.5±0.4
Cu/ZnO/Al <sub>2</sub> O <sub>3</sub> <sup>a</sup>	92.6±0.1	73.6±2.3	20.3±3.2	79.7±4.0	0.2±0.1	-	7.2±0.7
							4.4±0.9

<sup>a</sup> Reaction conditions: Gas hourly space velocity (GHSV) = 18,000  $\text{h}^{-1}$ , Steam-to-carbon ratio (S/C) = 2/1,  $T = 400$  °C. <sup>b</sup> TOF<sub>H<sub>2</sub></sub> based on the Cu<sup>0</sup> surface area and yield of H<sub>2</sub> at 350 °C. <sup>c</sup> TOF<sub>DME</sub> based on the total Cu surface areas and conversion of DME at 350 °C.





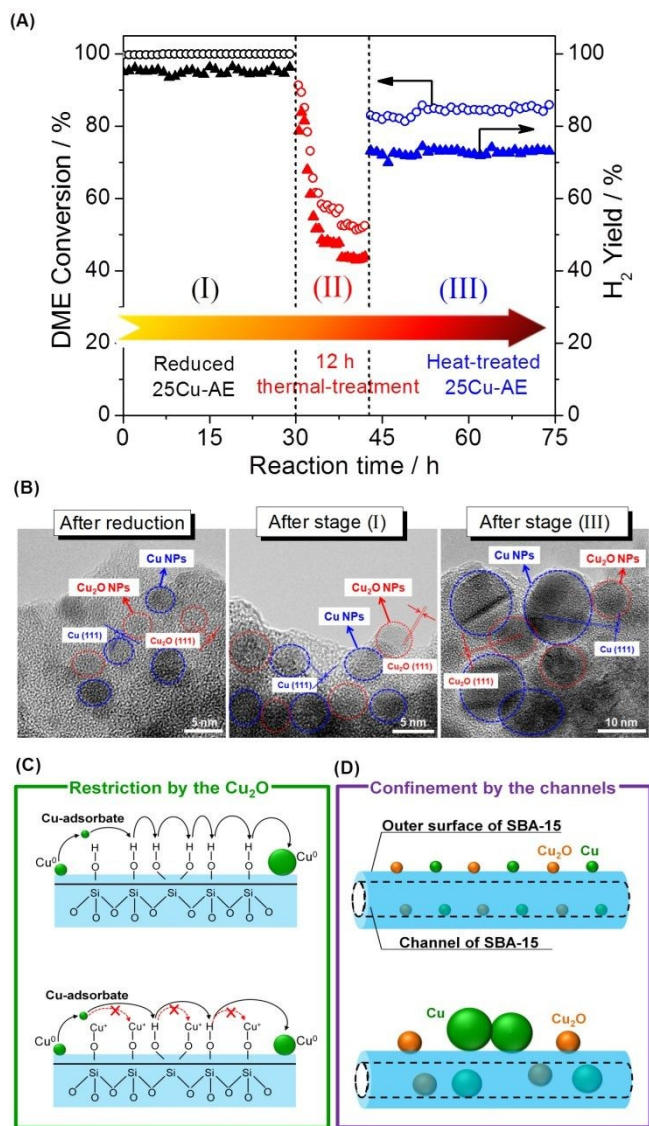


**Fig. 3** (A) Stabilities of 25Cu-AE upon thermal treatment. Reaction conditions: (I) and (III): GHSV = 18,000 h<sup>-1</sup>, S/C = 2/1 (mol/mol), T = 400 °C; (II): GHSV = 36,000 h<sup>-1</sup>, S/C = 2/1 (mol/mol), T = 450 °C; (B) TEM images of 25Cu-AE during the stability test; (C) Schematic representation of the restriction by the adjacent Cu<sub>2</sub>O; (D) Schematic illustration for the spatial confinement by the channels.

10%, and H<sub>2</sub> yield exceeding 95%, leading to a record-high H<sub>2</sub> production rate of 1145 mol<sub>H<sub>2</sub></sub> kg<sup>-1</sup><sub>cat</sub> h<sup>-1</sup> (Table S4), 6-fold than that of commercial CuZnAl.<sup>39</sup> The highest TOF<sub>H<sub>2</sub></sub> over 25Cu-AE reaches 0.147 s<sup>-1</sup>, about 2 and 10 times higher than those of as-prepared Cu/ZnO/Al<sub>2</sub>O<sub>3</sub> and 25Cu-IM, respectively (Table 1). Additionally, 25Cu-IM shows a lower H<sub>2</sub> yield and higher CO selectivity as compared with the Cu-AE catalysts, indicating that the latter's excellent catalytic activities probably lie in the presence of the Cu<sup>+</sup> species.

Fig. 3A displays the catalytic stability of 25Cu-AE, and Fig. 3B shows the TEM images at the corresponding stages. At stage I prior to the thermal treatment, the activity of 25Cu-AE shows no change while that of 25Cu-SiO<sub>2</sub> drops rapidly in Fig. S12. Intrinsically, unlike

the steady Cu NPs distribution of ~3.5 nm over 25Cu-AE (Fig. S13A), the Cu NPs over 25Cu-SiO<sub>2</sub> increase from ~4.1 to ~9.2 nm (Fig. S13B) after stage I.

As the reaction temperature (400 °C) is relatively lower than Tammann temperature of copper (407 °C), the thermal migration of copper atoms in the catalysts is difficult in absence of a reactive adsorbate. Thus, the copper particle growth in SR is probably mediated by mobile copper adsorbate species on support (Ostwald ripening).<sup>29</sup> The transport of Ostwald ripening Cu species depends upon the chemical nature of support surface. As evidenced by FTIR in Fig. S1A, the formation of copper phyllosilicates is accompanied by consuming surface hydroxyl groups, which is an efficient support functionalization to increase the distance between neighboring functional groups and consequently inhibits Cu<sup>0</sup> diffusion, as proposed in Fig. 3C. Accordingly, the structure of Cu surrounded by Cu<sub>2</sub>O in 25Cu-AE maximizes such restriction. Also, Cu<sub>2</sub>O NPs can function as physical spacer to isolate Cu<sup>0</sup> NPs.

After the thermal treatment (stage II), the DME conversion over 25Cu-AE drops to 84% but keep stable for another 30 h at stage III, meanwhile the TEM images of 25Cu-AE in Fig. 3B demonstrate a break of the surrounding structure of copper species. Herein, a bimodal size distribution of ~11.2 and ~5.8 nm is presented after stage III, which is attributed to the aggregated Cu species on the outer surface and in the channels, respectively (Fig. S13A). For 25Cu-SiO<sub>2</sub>, the catalytic performance substantially decreases at stage III. The corresponding Cu NPs noticeably aggregates as indicated by a distribution of ~15.0 nm after stage III (Fig. S13B). Thus, we conclude that the spatial restriction by the channels of SBA-15 can also participate to inhibit the aggregation of Cu<sup>0</sup> (Fig. 3D). Owing to such combined effects, 25Cu-AE exhibits a robust performance (DME conversion: 83.9%, H<sub>2</sub> yield: 72.7%) even after the severe thermal treatment.

We hypothesize that the high activity of Cu-AE results from a cooperative effect of their unique dual-sites of copper species. To gain more insight into this, the respective contributions from the Cu<sup>0</sup> and Cu<sup>+</sup> species are required to be clarified. Thus the catalysts containing pure Cu<sup>0</sup> and Cu<sup>+</sup> species are desired. However, the Cu<sup>0</sup> and Cu<sup>+</sup> always coexist in Cu-AE catalysts. For the above compared 25Cu-IM, its crystal size (29 nm) is much larger and less uniform than those of Cu-AE (< 10 nm) (Table S2). Moreover, the impregnation method inevitably brings the strong metal-support interaction to affect the chemical state and size distribution of copper. Consequently, we introduce a physical-sputtering method<sup>40</sup> to realize the homogeneously distributed metallic Cu nano-catalyst (Cu-SP) instead of 25Cu-IM for rigorous comparison and discussion. For Cu-SP, the TEM and H<sub>2</sub>-TPR results (Fig. S14) show that the copper NPs mainly exist as Cu<sup>0</sup>, which could be oxidized to Cu<sub>2</sub>O by N<sub>2</sub>O to obtain Cu-SP-N. Their physicochemical properties are listed in Table S5.

We quantify the surface density of Cu<sup>+</sup> and Cu<sup>0</sup> sites (Tables S2 and S5) to analyze their contributions toward the reaction. In Fig. 4A, the surface Cu<sup>0</sup> site density is observed to scale linearly with the formation rates of H<sub>2</sub> (*r*<sub>H<sub>2</sub></sub>) in group I and II independently, suggesting that the H<sub>2</sub> yield depends on the Cu<sup>0</sup> density with two different reaction paths. Whereas, there is no clear correlation between the *r*<sub>H<sub>2</sub></sub> and the total Cu density (Fig. 4B). Moreover, the higher superficial Cu<sup>+</sup>/(Cu<sup>0</sup>+Cu<sup>+</sup>) ratio (> 0.50) over the catalysts in



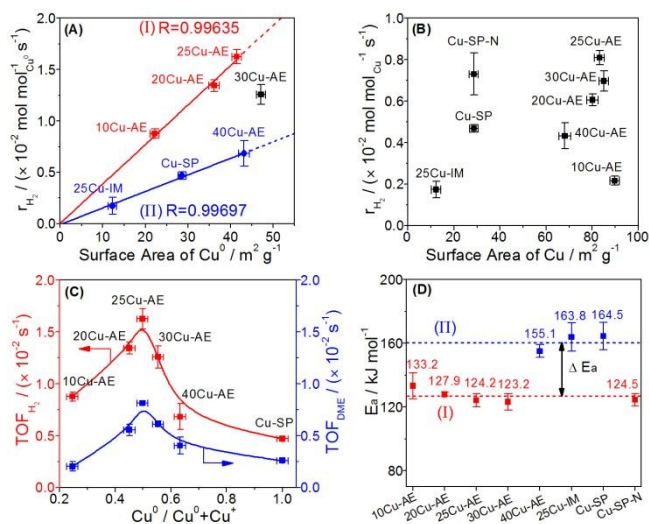


**Fig. 4** Correlation of the H<sub>2</sub> production rate based on Cu<sup>0</sup> sites or total Cu sites with (A) surface area of Cu<sup>0</sup>, and (B) total surface area of Cu; (C) Correlation of TOF of H<sub>2</sub> and DME with Cu<sup>0</sup>/(Cu<sup>0</sup> + Cu<sup>+</sup>) ratio; (D) Apparent activation energies of the catalysts.

group I than that (< 0.21) in group II, is probably the main reason for their superior performance. Thus, we conclude that Cu<sup>0</sup> is responsible for H<sub>2</sub> desorption, and sufficient Cu<sup>+</sup> can accelerate the reaction rate. In Fig. 4C, both the TOF<sub>DME</sub> and TOF<sub>H<sub>2</sub></sub> show a volcanic correlation with the increased Cu<sup>0</sup>/(Cu<sup>0</sup> + Cu<sup>+</sup>), and reach a maximum at the Cu<sup>0</sup>/(Cu<sup>0</sup> + Cu<sup>+</sup>) equal to 0.50 (25Cu-AE). The activation energies ( $E_a$ ) of the catalysts were calculated and classified into two

types in Fig. 4D: the lower value at ca. 125 kJ mol<sup>-1</sup> for 10Cu-AE, 20Cu-AE, 25Cu-AE and 30Cu-AE with sufficient Cu<sup>0</sup> sites (denoted as Cu<sup>0</sup>-suf); and the higher value at ca. 160 kJ mol<sup>-1</sup> for 25Cu-IM, Cu-SP and 40Cu-AE with sufficient Cu<sup>+</sup> sites (denoted as Cu<sup>+</sup>-suf). Interestingly,  $E_a$  dropped from 164.5 to 124.5 kJ mol<sup>-1</sup> when the Cu<sup>0</sup> sites in Cu-SP were oxidized to Cu<sup>+</sup> by N<sub>2</sub>O in Cu-SP-N. These results demonstrate the determinant role of the sufficient Cu<sup>+</sup> sites for reaction paths. Herein, 30Cu-AE follows the same reaction path with the other Cu<sup>+</sup>-suf catalysts, while its  $r_{H_2}$  is diverged from group I in Fig. 4A, which is probably ascribed to the excessive Cu<sup>0</sup> sites on 30Cu-AE for H<sub>2</sub> desorption. Summarily, we propose that there exist two reaction paths, and which to follow is determined by Cu<sup>+</sup>.

Thereafter, we evaluated the *in-situ* DRIFTS and temperature programmed surface reaction-mass spectroscopy (TPSR-MS) for methanol SR to validate the role of the copper species on the reaction path. In Fig. 5A, we observe the bands of Cu<sup>+</sup>-OCH<sub>3</sub> (methoxy) (1440 cm<sup>-1</sup>) over Cu<sup>+</sup>-suf and Cu<sup>0</sup>-OOCH (formate) (1345 cm<sup>-1</sup>) over Cu<sup>0</sup>-suf, respectively, which is also evidenced by the steady-state TPSR-MS (Fig. 5B, C). It suggests that the methoxy and formate groups on their corresponding catalysts are relatively stable, and their dehydrogenation affects the overall reaction rate. Importantly, the dioxomethylene (CH<sub>2</sub>O<sub>2</sub>) is also detected by TPSR-MS in Fig. 5C. Along with the kinetics and  $E_a$  discrimination from Fig. 4, these findings demonstrate the different rate-determining steps: methoxy dehydrogenation for Cu<sup>+</sup>-suf and formate dehydrogenation for Cu<sup>0</sup>-suf.

Then we collected time-resolved *in-situ* DRIFTS spectra of 25Cu-AE, Cu-SP and Cu-SP-N (Figs. S15-S17, Table S6) to draw the hypothetical mechanism. Over Cu<sup>+</sup>-suf, we assume that the Cu<sup>0</sup> sites are responsible for transferring atomic H and hydrogen

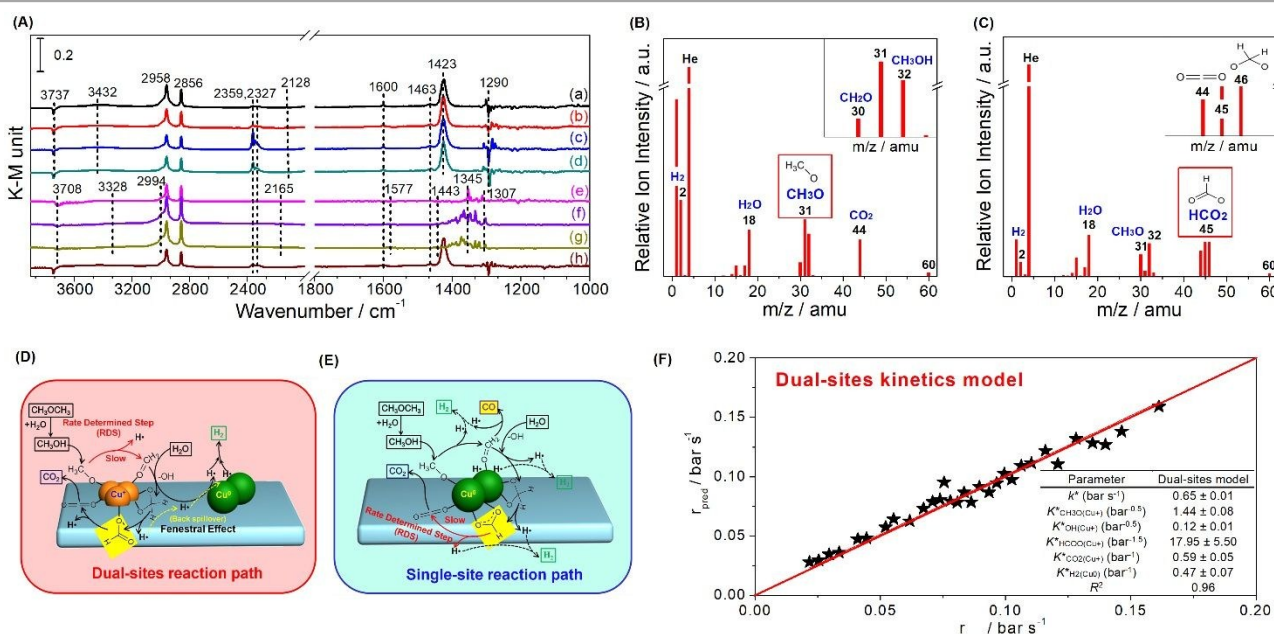


**Fig. 5** (A) Steady-state DRIFTS spectra for methanol SR on reduced (a) 10Cu-AE, (b) 20Cu-AE, (c) 25Cu-AE, (d) 30Cu-AE, (e) 40Cu-AE, (f) 25Cu-IM, and (g) Cu-SP, (h) Cu-SP-N; TPSR-MS spectra for methanol SR over the (B) reduced 25Cu-AE (Cu<sup>+</sup>-suf) and (C) Cu-SP (Cu<sup>0</sup>-suf) at 230 °C under steady-state conditions; The hypothetical reaction paths on the (D) dual-sites of copper species; and (E) single Cu<sup>0</sup> site; (F) Parity plots of microkinetic modeling for methanol SR over 25Cu-AE, and the inset is the fitting parameters given with confidence interval (± 5%) and stability index  $R^2$ .

desorption; and the Cu<sup>+</sup> sites are contributed to adsorbing oxygen-bonded intermediates.<sup>41</sup> From the *in-situ* DRIFTS results in Fig. S15, the catalytic cycle begins with the dissociative adsorption of methanol (1008, 1033 cm<sup>-1</sup>) on the surface. Then, dehydrogenation of the methoxy group (1440, 1423 cm<sup>-1</sup>) to formaldehyde occurs as the first barrier. Surface hydroxyls (3737 cm<sup>-1</sup>) immediately attack the formaldehyde, resulting in the formation of dioxomethylene as a reaction intermediate. Whereafter, it dehydrogenates into formate groups (1548, 1600 cm<sup>-1</sup>), and proceeds to dehydrogenate eventually to CO<sub>2</sub> (2359, 2327 cm<sup>-1</sup>), adsorbing in the form of monodentate carbonate species (1463 cm<sup>-1</sup>). All of H atoms produced by dehydrogenation migrate to the Cu<sup>0</sup> sites through support due to the fenestral effect (back spillover), and finally desorb as gaseous H<sub>2</sub>. We name it dual-sites reaction path (Fig. 5D). Over Cu<sup>0</sup>-suf in Fig. S16, the adsorption and transition of methanol (1010, 1030 cm<sup>-1</sup>), formaldehyde (1736 cm<sup>-1</sup>), dioxomethylene, formate (1345, 1577 cm<sup>-1</sup>) and carbonate (1371 cm<sup>-1</sup>) occurs on the Cu<sup>0</sup> sites alone (Fig. 5E), consistently with the reported DFT calculations on Cu(111).<sup>42</sup> In this case, H is competitively adsorbed with oxygenates intermediates, thereby readily meeting the second barrier at formate dehydrogenation and inhibiting the overall reaction rate.

Interestingly, in Fig. 5A, monodentate formate (1600 cm<sup>-1</sup>), considered to be more active in deep dehydrogenation,<sup>43</sup> tends to form on Cu<sup>+</sup>-suf, while both monodentate (1577 cm<sup>-1</sup>) and bidentate (1345 cm<sup>-1</sup>) species appear on Cu<sup>0</sup>-suf. Cu<sup>+</sup> sites may functionalize as the electrophilic sites to readily electrostatically adsorb the negative electron of O-C in formate, thereby forming more active monodentate formate to overcome the formate dehydrogenation barrier. Thus, we intrinsically reveal that the rate-determining step of the dehydrogenation of methoxy or formate relies on the valence state of Cu.

Through the evaluation on a recycle fixed-bed reactor (Fig. S18), a microkinetic model for methanol SR over 25Cu-AE was established to verify the reliability of our proposed dual-sites reaction path (See details in Experimental section of ESI). In this model, the competitive adsorption of oxygenates and dissociative adsorption of hydrogen occur on Cu<sup>+</sup> and Cu<sup>0</sup> sites, respectively. The dehydrogenation of the methoxy group on Cu<sup>+</sup> sites is the rate-determining step, and thus all of the other elemental reactions are in thermodynamic equilibrium. As expected, the experimental data and the dual-sites microkinetic prediction are in good agreement (Fig. 5F).

## Conclusions

In summary, we successfully design a dual Cu reforming system with a record-high and robust H<sub>2</sub> production rate of 1145 mol kg<sup>-1</sup> cat h<sup>-1</sup>, and describe new insights into the fundamental understanding for Cu-catalyzed SR. In fact, there exist two kinds of distinct rate-determining step: methoxy dehydrogenation for Cu<sup>+</sup>-suf and formate dehydrogenation for Cu<sup>0</sup>-suf. Cu<sup>+</sup> may function as the electrophilic sites to adsorb the negative electron of O-C in formate, thereby more readily forming active monodentate formate. This can intrinsically accelerate the overall reaction rates. Moreover, the surrounding Cu<sub>2</sub>O and nano-channels of SBA-15 can inhibit the aggregation of metallic Cu species during SR. Our design provides a

commercially achievable reforming system for fuel cells, and paves a new way to related reaction mechanism investigations.

## Conflicts of interest

The authors declare no conflict of interest.

## Author contributions

X.G.L., J.L.G. and K.M. conceived the idea; K.M., J.L.G., Y.T., Z.J.Z., Q.P.C. and T.D. carried out the experiments; N.T. and T.A. prepared the sputtered catalysts; J.Z., L.R.Z. and Z.J. helped to collect XAFS data; X.G.L., J.L.G. and K.M. analyzed the experimental data and wrote the manuscript. X.G.L. and J.L.G. supervised the whole project. All authors participated in discussions of the research.

## Acknowledgements

This work is supported by National Key R&D Program of China (2016YFB0600901), National Natural Science Foundation of China (Nos. 21476159, 21476160, 21525626) and the Program of Introducing Talents of Discipline to Universities (No. B06006). We gratefully thank Prof. Ming Meng for his help on this work. We also acknowledge the staff members of the 1W1B station in Beijing Synchrotron Radiation Facility (BSRF) and BL14W1 station in Shanghai Synchrotron Radiation Facility (SSRF) for their assistance in the XAFS experiments.

## Notes and references

- M. Dresselhaus and I. Thomas, *Nature*, 2001, **414**, 332-337.
- U. Eberle, B. Muller and R. von Helmolt, *Energy Environ. Sci.*, 2012, **5**, 8780-8798.
- S. Krishnan and F. A. Armstrong, *Chem. Sci.*, 2012, **3**, 1015-1023.
- R. D. Cortright, R. Davda and J. A. Dumesic, *Nature*, 2002, **418**, 964-967.
- L. Schlapbach and A. Züttel, *Nature*, 2001, **414**, 353-358.
- P. Leung, A. Tsolakis, J. Rodriguez-Fernandez and S. Golunski, *Energy Environ. Sci.*, 2010, **3**, 780-788.
- C. Dang, Y. Li, S. M. Yusuf, Y. Cao, H. Wang, H. Yu, F. Peng and F. Li, *Energy Environ. Sci.*, 2018, **11**, 660-668.
- X. Zhao, H. Zhou, V. S. Sikarwar, M. Zhao, A.-H. A. Park, P. S. Fennell, L. Shen and L.-S. Fan, *Energy Environ. Sci.*, 2017, **10**, 1885-1910.
- T. A. Semelsberger, R. L. Borup and H. L. Greene, *J. Power Sources*, 2006, **156**, 497-511.
- J. Sun, G. Yang, Y. Yoneyama and N. Tsubaki, *ACS Catal.*, 2014, **4**, 3346-3356.
- R. Luque, L. Herrero-Davila, J. M. Campelo, J. H. Clark, J. M. Hidalgo, D. Luna, J. M. Marinas and A. A. Romero, *Energy Environ. Sci.*, 2008, **1**, 542-564.
- K. Faungnawakij, R. Kikuchi, N. Shimoda, T. Fukunaga and K. Eguchi, *Angew. Chem. Int. Ed.*, 2008, **47**, 9314-9317.
- D. Li, X. Li and J. Gong, *Chem. Rev.*, 2016, **116**, 11529-11653.
- D. R. Palo, R. A. Dagle and J. D. Holladay, *Chem. Rev.*, 2007, **107**, 3992-4021.
- H. Oguchi, T. Nishiguchi, T. Matsumoto, H. Kanai, K. Utani, Y. Matsumura and S. Imamura, *Appl. Catal. A*, 2005, **281**, 69-73.
- Y. Matsumura and H. Ishibe, *J. Catal.*, 2009, **268**, 282-289.



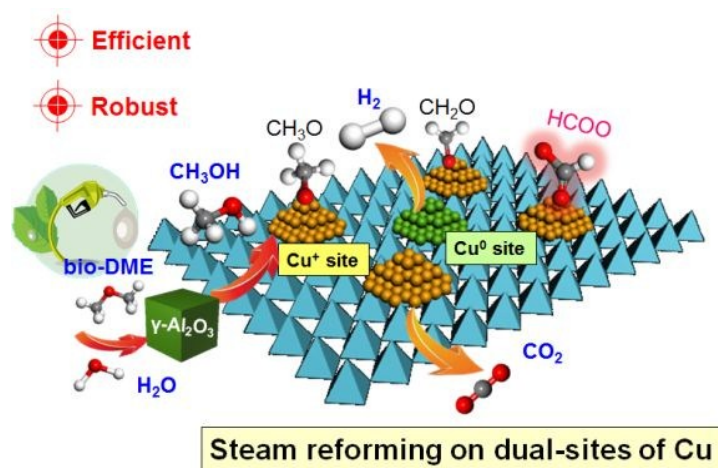


- 17 Y. Matsumura and H. Ishibe, *Appl. Catal. B*, 2009, **86**, 114-120.
- 18 I. Ritzkopf, S. Vukojević, C. Weidenthaler, J.-D. Grunwaldt and F. Schüth, *Appl. Catal. A*, 2006, **302**, 215-223.
- 19 Y. Liu, T. Hayakawa, K. Suzuki, S. Hamakawa, T. Tsunoda, T. Ishii and M. Kumagai, *Appl. Catal. A*, 2002, **223**, 137-145.
- 20 X. Wang, K. Ma, L. Guo, Y. Tian, Q. Cheng, X. Bai, J. Huang, T. Ding and X. Li, *Appl. Catal. A*, 2017, **540**, 37-46.
- 21 C. Rameshan, W. Stadlmayr, S. Penner, H. Lorenz, N. Memmel, M. Hävecker, R. Blume, D. Teschner, T. Rocha, D. Zemlyanov, A. Knop-Gericke, R. Schlögl and B. Klötzer, *Angew. Chem. Int. Ed.*, 2012, **51**, 3002-3006.
- 22 K. M. K. Yu, W. Tong, A. West, K. Cheung, T. Li, G. Smith, Y. Guo and S. C. E. Tsang, *Nat. Commun.*, 2012, **3**, 1230.
- 23 J. Huang, T. Ding, K. Ma, J. Cai, Z. Sun, Y. Tian, Z. Jiang, J. Zhang, L. Zheng and X. Li, *ChemCatChem*, 2018, **10**, 3862-3871.
- 24 H. Xi, X. Hou, Y. Liu, S. Qing and Z. Gao, *Angew. Chem. Int. Ed.*, 2014, **53**, 11886-11889.
- 25 K. Ma, Z. Cui, Z. Zhang, J. Huang, Z. Sun, Y. Tian, T. Ding and X. Li, *ChemCatChem*, 2018, **10**, 4010-4017.
- 26 L. F. Chen, P. J. Guo, M. H. Qiao, S. R. Yan, H. X. Li, W. Shen, H. L. Xu and K. N. Fan, *J. Catal.*, 2008, **257**, 172-180.
- 27 J. Gong, H. Yue, Y. Zhao, S. Zhao, L. Zhao, J. Lv, S. Wang and X. Ma, *J. Am. Chem. Soc.*, 2012, **134**, 13922-13925.
- 28 H. Yue, Y. Zhao, S. Zhao, B. Wang, X. Ma and J. Gong, *Nat. Commun.*, 2013, **4**.
- 29 R. Van den Berg, T. E. Parmentier, C. F. Elkjær, C. J. Gommès, J. Sehested, S. Helveg, P. E. de Jongh and K. P. de Jong, *ACS Catal.*, 2015, **5**, 4439-4448.
- 30 J. Fan, X. Jiang, H. Min, D. Li, X. Ran, L. Zou, Y. Sun, W. Li, J. Yang, W. Teng, G. Li and D. Zhao, *J. Mater. Chem. A*, 2014, **2**, 10654-10661.
- 31 T. Tsoncheva, V. Dal Santo, A. Gallo, N. Scotti, M. Dimitrov and D. Kovacheva, *Appl. Catal. A*, 2011, **406**, 13-21.
- 32 X. Wang, J. Zhuang, J. Chen, K. Zhou and Y. Li, *Angew. Chem. Int. Ed.*, 2004, **116**, 2051-2054.
- 33 A. Ungureanu, B. Dragoi, A. Chiriac, C. Ciotonea, S. Royer, D. Duprez, A. S. Mamede and E. Dumitriu, *ACS Appl. Mater. Interfaces*, 2013, **5**, 3010-3025.
- 34 L. F. Chen, P. J. Guo, L. J. Zhu, M. H. Qiao, W. Shen, H. L. Xu and K. N. Fan, *Appl. Catal. A*, 2009, **356**, 129-136.
- 35 A. Marchi, J. Fierro, J. Santamaria and A. Monzon, *Appl. Catal. A*, 1996, **142**, 375-386.
- 36 A. Yin, X. Guo, W. L. Dai and K. Fan, *J. Phys. Chem. C*, 2009, **113**, 11003-11013.
- 37 X. Zheng, H. Lin, J. Zheng, X. Duan and Y. Yuan, *ACS Catal.*, 2013, **3**, 2738-2749.
- 38 L. S. Kau, D. J. Spira-Solomon, J. E. Penner-Hahn, K. O. Hodgson and E. I. Solomon, *J. Am. Chem. Soc.*, 1987, **109**, 6433-6442.
- 39 Y. Tanaka, R. Kikuchi, T. Takeguchi and K. Eguchi, *Appl. Catal. B*, 2005, **57**, 211-222.
- 40 X. G. Li, C. Liu, J. Sun, H. Xian, Y. S. Tan, Z. Jiang, A. Taguchi, M. Inoue, Y. Yoneyama, T. Abe and N. Tsubaki, *Sci. Rep.*, 2013, **3**, 2813.
- 41 S. Lin, D. Xie and H. Guo, *J. Phys. Chem. C*, 2011, **115**, 20583-20589.
- 42 S. Lin, R. S. Johnson, G. K. Smith, D. Xie and H. Guo, *Phys. Chem. Chem. Phys.*, 2011, **13**, 9622-9631.
- 43 A. Haghofer, D. Ferri, K. Föttinger and G. n. Rupprechter, *ACS Catal.*, 2012, **2**, 2305-2315.

View Article Online  
DOI: 10.1039/C9SC00015A







View Article Online  
DOI: 10.1039/C9SC00015A

This paper describes how  $\text{Cu}^+$  species act as electrophilic sites to facilitate the adsorption and activation of the formate and restrict the Ostwald ripening of Cu species, leading to an efficient and robust steam reforming of bio-DME.

